RSC Advances

ROYAL SOCIETY OF CHEMISTRY

www.rsc.org/advances

Branched ultra-fine nickel oxide/ manganese dioxide core-shell nanosheet arrays for electrochemical capacitor

Yanhong Li[a], Huarong Peng[b], Chao Zhang[a], Mengsha Chu[a], Peng Xiao[*a] and Yunhuai Zhang[*b]

[a] *College of Physics, Chongqing University, Chongqing, 400030, P. R. China*

[b] *College of Chemistry and Chemical Engineering, Chongqing University, Chongqing, 400030, P. R. China*

[*] Corresponding author.

Tel: +86-15823038874; Fax: +86-023-65102031

E-mail: xiaopeng@cqu.edu.cn; xp2031@163.com

Abstract

We demonstrate the fabrication of ultra-fine hierarchical NiO@MnO_2 core-shell nanosheets arrays on carbon fiber paper via a facile and two-step hydrothermal method as the electrode for supercapacitors. Owing to the unique hierarchical core-shell heterostructured nanosheets arrays configuration and synergetic contribution from the NiO core and MnO_2 shell, the as-prepared hybrid nanosheets arrays exhibited a high specific capacitance of 494.8 F g^{-1} and good rate capability, which are better than that of the obtained individual component of NiO nanosheets. More importantly, the asymmetric supercapacitor, composed of NiO@MnO_2 core-shell nanosheets arrays as positive electrode and activated carbon as negative electrode delivers a specific capacitance of 86.3 F g^{-1} and reaches up to an energy density of 30.6 Wh kg^{-1} and power density of 400 W kg^{-1}. The improved performance of NiO@MnO_2 core-shell nanosheet arrays demonstrates that rational design of electrode structure is an effective way to fabricate high-performance electrode for supercapacitor.

1. Introduction

Under the circumstance of the increasingly exhausting of non-renewable resources and the worsening environmental pollution, energy conversion and storage is unquestionably becoming one of the great challenges. In order to exploit the high efficiency energy storage devices, which are able to store large quantities of electrical energy and can be rapidly charged/discharged,[1-4] much efforts are urgently devoted to the development of novel electrode materials. It is now well recognized that materials with multifunctional properties or a hybrid combination of various nanomaterials are expected to meet the on-board energy demands and are widely prepared dut to their superior properties than each component.[5,6] Types of hybrid nanostructures include (i) segmanted hybrid materials, (ii) core-shell hybrid materials, (iii) 0-D (zero-dimensionality) nanoparticle-decorated 1-D nanostructures.[5] Particularly, ordered arrays of hybrid core-shell nanostructures can effectively improve the electrochemical reversibility and have advantage of efficient electron transfer between current collector and individual electrode material and fast ion transport/easy electrolyte access to electrode due to available void volume between adjacent nanostructured electrodes. Thus, enhanced properties or novel useful properties can be delivered when single-phase nanomaterial in becoming part of the hybrid combination.[6,7]

Transition metal oxides have long been studied as potential electrode materials for lithium ion batteries and pseudocapacitors because of the ease of large-scale fabrication and their rich redox reactions involving different ions, which contributes to high specific capacitances, such as CoO_x,[8] NiO,[9-11] MnO_2,[12-16] Fe_2O_3[17,18] and V_2O_5.[19] Among various candidate materials, NiO and MnO_2 are widely investigated as electrode materials for supercapacitor due to their considerable theoretical specific (2574 F g^{-1} for NiO[17] and 1370 F g^{-1} for MnO_2[11,12]) and their abundant resources. However,

the poor capacity retention of NiO and low conductivity of MnO_2 (10^{-5}–10^{-6} S cm^{-1}) hinder their practical application.[14,20,21] In this regard, one attractive concept is to incorporate MnO_2 or NiO into conductive carbon-based materials[22-26] (carbon nanotube, graphene and carbon aerogels) or conducting coating[11,16,27] (metals, carbon and polymers) to address this issue. For instance, Zhang et al.[25] prepared MnO_2 electrochemical reduced-GO electrodes which exhibited a high specific capacitance of 422.5 F g^{-1}. By taking advantages of graphene oxide (GO), manganese ions can transport more easily onto the surface of GO, which will effectively increase the active surface of MnO_2 and hence enhance the energy storage property. However, in this case, the energy density is generally sacrificed to achieve better rate capability and cycling stability. Another alternative way is to synthesize hybrid core-shell nanostructures aligning on current collectors as binder-free electrodes for electrochemical capacitors which can ensure the more efficient ion diffusion and faster electron transport.[7,28-34] Improved performance has been achieved in these hybrid materials due to its elegant synergy between individual component and the facility of efficient electron transfer between current collector and active materials.[29,35-37] Besides, the voids volume between neighboring nanostructured arrays can also promote fast ion transport and allow easy accessibility of electrolyte.[7,34] For example, MnO_2 nanostructure deposited onto 3-D nickel nanocone arrays with a high specific capacitance (632 F g^{-1}) and outstanding mechanical robustness was reported by Su's group.[27] In addition, the Ni@NiO core-shell electrode reported by Lu' group shows ultrahigh capacitance of 2.0 F cm^{-2} and super-long cyclic stability.[35] A key challenge in this direction is to build up an integrated ultra-fine smart architecture where structural features and electro-activities of individual component are fully manifested. In this regard, design of electrode materials with 2-D would be an ideal solution compared with widely studied 1-D structural configuration, which could offer more exposed active

site than the latter.

Herein, we reported the design and synthesis of hierarchical NiO@MnO_2 core shell nanosheets arrays on carbon fiber paper (CFP) as binder free-electrode for electrochemical capacitors. We choose ultra-fine NiO nanosheets as scaffold for the growth of branched MnO_2 shell. By elaborate design and rational combination of NiO and MnO_2 nanostructure, the NiO@MnO_2 nanosheets could deliver an areal specific capacitance of 1.0 F cm^{-2} (494.8 F g^{-1}). In addition, the asymmetric supercapacitor composed of NiO@MnO_2 electrode and commercial activated carbon delivers an maximum energy density of 30.6 Wh kg^{-1} and power the density 6400 W kg^{-1}.

2. Experimental

2.1 Preparation of NiO nanosheets arrays

All the chemicals were analytical grade and were used without any further purification. The sample was prepared by a two-step hydrothermal method. Typically, a aqueous solution containing 0.05 M $Ni(Ac)_2 \cdot 4H_2O$ and 0.15 M Hexamethylenetetramine (HMT) was transferred to a Teflon-lined stainless autoclave with CFP. After 5 h growth at 120℃, the precursor were washed with ethanol and distilled water before dried. Finally, NiO nanosheet were obtained after annealed in air atmosphere at 350□ for 2 h. The mass loading of NiO is ~0.3 mg cm^{-2}.

2.2 Preparation of ultran-fine core-shell NiO/MnO_2 nanosheet arrays

For the synthesis of core-shell NiO/MnO_2 nanosheet, the obtained NiO was further put into a Teflon-lined stainless autoclave containing 0.04 M $KMnO_4$ aqueous solution which was kept at 160 □ for 30 minutes. Finally, core-shell NiO/MnO_2 nanosheet arrays were obtained after drying at room temperature. The mass loading of NiO@MnO_2 is 2.1 mg cm^{-2}.

2.3 Characterizations and electrochemical measurements

The morphologies and structures of samples were characterized by field-emission scanning electron microscopy (FESEM, JSM-7800F) equipped with an energy-dispersive X-ray spectroscopy detector (EDS), X-ray diffraction (XRD, shimadzu 2D-3AX, Cu Kα radiation, λ=1.5418 Å) and transmission electron microscopy (TEM, Tecnai G2 F20 U-TWIN). The porous structures of materials were characterized by Nitrogen adsorption-desorption measurements (Micromeritics ASAP 2020) along with the Brunauer-Emmet-Teller (BET) specific surface area and Barrett-Joyner-Halenda (BJH) pore size distribution.

Three-electrode electrochemical measurements were carried out at ambient temperature in 1M KOH aqueous solution with active materials supported on CFP (1×1 cm^2), a Pt foil and Ag/AgCl (saturated KCl) electrode used as working electrode, counter electrode and reference electrode, respectively. All potentials were referred to the reference electrode. For the tests in two-electrode system, both of the electrodes have the geometrical area of 1 cm^2 which were separated by a glass fiber filter paper with 1 M KOH aqueous solution as electrolyte. The NiO/MnO_2 nanosheets arrays were the positive electrode and the commercial activated carbon (AC) prepared by mixing active carbon, acetylene black and 60 wt% PTFE in a 80 : 15 : 5 mass ratio was negative electrode, which was then pressed onto nickel foam and dried overnight. The electrochemical performance of the samples were performed on a CHI66D (Chenhua, Shanghai) workstation for cyclic voltammetry (CV), chronopotentiometry (CP) tests and electrochemical impedance spectroscopy (EIS). The electrochemical impedance spectroscopy (EIS) tests were carried out at open circuit potential applying 5 mV ac voltage in the frequency range from 100 kHz to 0.01 Hz. The galvanostatic charge-discharge cycling tests were conducted using a LAND battery program-control test system (LAND, Wuhan).

3. Results and discussion

3.1 Morphology and structure characterizations

Fig. 1a illustrates the XRD patterns of NiO and hierarchical NiO@MnO_2 core-shell arrays. Apart from the peaks located at 26.6° and 54.5° for substrate, the peaks located at 37.3°, 43.4° and 62.8° can be indexed to the of NiO (JCPDS 44-1159). For NiO@MnO_2 core-shell arrays, two new peaks appear, which can be indexed to (002) and (020) or (-312) peaks for MnO_2 (JCPDS 80-1098). Besides, the peak located at 37.3° became broad and shifted to a lower degree direction, which may be due to the overlap of (101) plane NiO and (-111) plane of MnO_2. It is worth noting that due to the second growth of MnO_2 on NiO, the (012) and (110) peaks of NiO became weak and almost disappeared. The XRD results indicate the coexistence of NiO and MnO_2. The successful growth of MnO_2 is also evidenced by EDS in Fig. 1b, which is in accordance with XRD results. It shows that the sample contains Ni, Mn and O with and a trace presence of K, arising from the residual K in the interlayer of MnO_2.

The SEM images of the as prepared samples with different magnifications are presented in Fig. 2. It can be observed that NiO with ultra-fine nanosheets are grown uniformly on CFP, forming a 3D hierarchical structure. Further after the reaction in $KMnO_4$, NiO nanosheet was covered with uniform and ultra-thin MnO_2 nanosheets, which are thought to have developed naturally as a result of the crystallographic habit of birnessite-type MnO_2, building a 2D nanosheet@nanosheet core-shell unique architecture. As can be seen from Fig. 2b, the NiO ultrathin sheets are converted to thick walls and the MnO_2 layer on the surface of NiO is also constructed by small ultrathin sheets. The detailed structural information of hierarchical NiO@MnO_2 core–shell was further investigated by TEM. Figure 2c and d show a typical transmission electron microscopy (TEM) image at different

magnification. The results confirm the uniform growth of MnO_2 on NiO and their sheet-like morphology. The high-resolution TEM (HRTEM) image shown in Fig. 2e reveals the interplanar spacing of 0.212, 0.252 and 0.253 nm for two curling nanosheets, corresponding to the (-112), (200) and (-201) plane of birnessite-type MnO_2. Besides, the typical diffraction rings in SAED pattern shows (113) and (024) plane of NiO and (114) and (201) plane of MnO_2. SAED results together with the HRTEM images, demonstrates a polycrystalline nature of NiO@MnO_2.

To further investigate the surface and porous properties of the hierarchical NiO@MnO_2 core-shell arrays, the N_2 adsorption-desorption isotherm pores were measured. Brunauer-Emmett-Teller (BET) and Barret-Joyner-Halenda (BJH) methods are employed to calculate the surface area value and pore size distribution of the samples, respectively. As shown in Fig. 3, it can be seen that the N_2 adsorption-desorption curves of NiO@MnO_2 core-shell arrays has a hysteresis loop in a relative pressure (P/P_0) range of 0.5-1.0, characteristic of type-IV isotherms.[32,33] The N_2 adsorption-desorption isotherm results indicate that NiO@MnO_2 core-shell arrays electrode exhibit a BET surface area of 40.3 m^2 g^{-1}. Barrett-Joyner-Halenda (BJH) pore size distribution further demonstrates that the average pore size was ~3.3 nm.

3.2. Electrochemistry measurements

The electrochemical performance of as-prepared hierarchical NiO@MnO_2 core-shell nanosheets structure is evaluated as binder-free electrodes for supercapacitors by cyclic voltammetry (CV) and galvanostatic charge-discharge measurements carried out in 1 M KOH. Fig. 4a shows the representative CV curves of NiO@MnO_2 core-shell nanosheets and pristine NiO nanosheets arrays at the scan rate of 10 mV s^{-1}. The CV curve of NiO nanosheets shows a pair of redox peaks, which correspond to the conversion between different nickel oxidation states.[11,12] For NiO@MnO_2

core-shell nanosheets, a pair of redox peaks with a larger enclosed rectangle shaped CV curve can also be observed, revealing the pseudocapacitive characteristics and its higher specific capacitance.[31,34] CV curves of NiO@MnO_2 with various sweep rates ranging from 5 to 50 mV s^{-1} are plotted in Fig. 4b. With the increase of sweep rates, the current density increases and the positions of anodic and cathodic peaks shift to a more anodic and cathodic direction, respectively, indicating the fast redox reactions occur at electro-active material/electrolyte interface. Fig. 4c show the galvanostatic charge-discharge profiles tested at different current density. The observation of nearly symmetric potential-time curves at all current densities implies the high charge-discharge coulombic efficiency and low polarization of the unique electrode. The specific capacitance retention of NiO@MnO_2 nanosheets and pristine NiO nanosheets arrays calculated from the galvanostatic charge-discharge curves as a function of scan rate is shown in Fig. 4d. It is obvious that the specific capacitances decrease with increasing scan rate which is due to less number of ions lodged in the electrode at higher scan rate that leads to low utilization of active materials. The SCs of the NiO@MnO_2 electrode calculated based on the charge-discharge curves is much higher than that of pristine NiO nanosheets under the same current density. In addition, NiO demonstrated a better rate capability compared with NiO@MnO_2 when the current density varies from 2 to 8 mA cm^{-2}, which might be due to a low utilization of active materials for NiO@MnO_2 with the increasing of current density. Furthermore, to verify the results, electrochemical impedance spectroscopy (EIS) tests were carried out at open circuit potential applying 5 mV ac voltage in the frequency range from 100 kHz to 0.01 Hz. The Nyquist plots of the NiO and NiO@MnO_2 electrodes are illustrated in Fig. 4e. It is can be seen that NiO@MnO_2 demonstrates a smaller internal resistance than that of NiO nanosheets. In addition, there are two semicircles at high frequency region, corresponding to the charge-transfer

resistance (R_{ct}) at the NiO core/MnO_2 shell and MnO_2/electrolyte interface, resulting in higher charge-transfer resistance than that of NiO. That is why the rate capability of NiO is better than that of NiO@MnO_2 when the discharge current density changes from 2 mA cm^{-2} to 8 mA cm^{-2} as exhibited in Fig. 4d. Cycling performance is a key factor in determining the supercapacitors for many practical applications. In this study, a long-term repeated charge-discharge cycling tests of the as-synthesized NiO@MnO_2 conducted at a constant current density of 20 mA cm^{-2} were employed. The results and charge-discharge curves for the last 17 cycles are shown in Fig. 4f. It can be seen that the specific capacitance retention of the electrode materials increases around 400th cycle and then gradually decreases, indicating the presence of an activation process of the electrodes at the beginning of galvanostatic charge-discharge test.[28] During this process, the electrode will be fully activated through the intercalation and de-intercalation of ions, resulting in the increase of active points inside the electrode materials, hence enhancing the specific capacitance. The hybrid core/shell nanowires array exhibits capacitance retention of 78% after 10000 cycles. The electrochemical properties of NiO@MnO_2 here is better than those similar reported materials, such as TiO_2 NW@MnO_2 NS (120 F g^{-1}, 0.1 A g^{-1}),[14] Co_3O_4 NW@MnO_2 NS (384.3 F g^{-1}, 1 A g^{-1}),[33] Ti@MnO_2 (467.8 F g^{-1}, A g^{-1}),[30] and Ni@MnO_2 (304 F g^{-1}, 2 A g^{-1}).[38] The improved performance is mainly attributed to the unique core shell structure of NiO@MnO_2 composed of two dimensional nanosheets.

To further assess the application value of the NiO@MnO_2 core shell NSAs, we fabricated an asymmetric supercapacitor, consisting of a battery-type Faradic electrode (positive electrode) as the energy source and a capacitor-type electrode (negative electrode) as the power source, which can exhibit higher energy density than that of symmetric ones due to the extended operating voltage.[10]

$NiO@MnO_2$ and commercial activated carbon were employed as positive electrode and negative electrode, respectively, with 1 M KOH solution as the electrolyte and one piece of filter paper as the separator. In order to obtain the maximum performance of the device, the charge balance between the two electrodes was considered based on the three-electrode electrochemical measurements of both $NiO@MnO_2$ and AC electrodes. The whole mass loading of the asymmetric capacitor is ~4.8 mg. The electrochemistry test results are presented in Fig. 5. As expected, CV curves of the device at different potential window (Fig. 5b) shows that the cell voltage could be extended to 1.6 V. Fig. 5b displays the CV curves of the device at different scan rates. All the curves exhibit relatively rectangular shape, indicating its good charge-discharge properties and rate capability. Galvanostatic charge-discharge tests (Fig. 5c) were employed to calculate the energy density and power density of the supercapacitor and Ragone plot at different current densities was obtained (Fig. 5e). A specific capacitance of 86.3 F g^{-1} is obtained based on the total mass active materials ($NiO@MnO_2$ and active carbon). An energy density of 30.6 Wh kg^{-1} is achieved at the power density of 400 W kg^{-1} and still remains 18.4 Wh kg^{-1} at high power density of 6.4 kW kg^{-1}, which demonstrates its superiority in retention of energy density. Fig. 5f reveals the cycling life and coulomb efficiency of the asymmetric supercapacitor at the current density of 4 A g^{-1}. It retains 98.3% of its initial capacitance after 10000 cycles, which highlights the capability of the hierarchical $NiO@MnO_2$ core-shell NSAs in real application.

4. Conclusion

In summary, we demonstrated the rational design and fabrication of hierarchical hybrid $NiO@MnO_2$ core-shell NSAs on CFP by a facile and two-step hydrothermal approach as electrode for supercapacitor applications. The NiO nanosheets function as scaffold to anchor ultra-thin MnO_2

nanosheets, leading to a well-designed hybrid architecture. The as-prepared hierarchical nanostructure exhibits improved electrochemical performance than the individual parts, which can be ascribed to the elaborate NiO nanosheets scaffold and the high specific surface area provided by branched ultra-thin MnO_2 shell as well as synergetic contribution from the porous NiO nanosheets core and the ultrathin MnO_2 shell. The as-prepared electrode delivers high capacitance of 494.8 F g^{-1} and desirable rate performance and electrochemical stability (78% retention after 10000 cycling test). In addition, a maximum energy density of 30.6 Wh kg^{-1} and power density of 6.4 kW kg^{-1} is achieved in a asymmetric supercapcitor where NiO@MnO_2 and active carbon was employed as positive and negative electrodes, respectively.

Acknowledgments

This work was supported by the fundamental research funds for the Central Universities (Project No. 106112015CDJZR305501) and the sharing of Chongqing University's large-scale equipment.

References

[1] P. Simon and Y. Gogotsi, *Nat. Mater.*, 2008, **7**, 845.

[2] J. Yan, Q. Wang, T. Wei and Z. J. Fan, *Adv. Energy Mater.*, 2014, **4**, 1300816.

[3] M. H. Yu, Y. Han, X. Y. Cheng, L. Hu, Y. X. Zeng, M. Q. Chen, F. L. Cheng, X. H. Lu and Y. X. Tong, *Adv. Mater.*, 2015, **27**, 3085.

[4] W. Wang, W. Y. Liu, Y. X. Zeng, Y. Han, M. H. Yu, X. H. Lu and Y. X. Tong, *Adv. Mater.*, 2015, **27**, 3572.

[5] A. L. M. Reddy, S. R. Gowda, M. M. Shaijunmon and P. M. Ajayan, *Adv. Mater.*, 2012, **24**, 5045.

[6] J. Jiang, Y. Y. Li, J. P. Liu, X. T. Huang, C. Z. Yuan, X. W. Lou, *Adv. Mater.,* **24** (2012) 5166.

[7] J. P. Liu, J. Jiang, C. W. Cheng, H. X. Li, J. X. Zhang, H. Gong and H. J. Fan, *Adv. Mater.*, 2011, **23**, 2076.

[8] H. Q. Sun, H. M. Ang, M. O. Tade and S. B. Wang, *J. Mater. Chem. A*, 2013, **1**, 14427.

[9] M. Chiku, M. Toda, E. Higuchi and H. Inoue, *J. Power Sources*, 2015, **286**, 193.

[10] X. Y. Yan, X. L. Tong, J. Wang, C. W. Gong, M. G. Zhang and L. P. Liang, *J. Alloys Comp.*, 2014, **593**, 184.

[11] X.-J. Ma, L.-B. Kong, W.-B. Zhang, M.-C. Liu, Y.-C. Luo and L. Kang, *RSC Adv.*, 2014, **4**, 17884.

[12] H. H. Xu, X. L. Hu, H. L. Yang, Y. M. Sun and C. C. Hu, *Adv. Energy Mater.*, 2014, **5**, 1401882.

[13] F. Li, Y. X. Zhang, M. Huang, Y. Xing and L. L. Zhang, *Electrochim. Acta*, 2015, **154**, 329.

[14] Y. X. Zhang, M. Kuang, X. D. Hao, Y. Liu, M. Huang, X. L. Guo, J. Yan, G. Q. Han and J. Li, *J. Power Sources*, 2014, **270**, 675.

[15] F. Li, Y. Xing, M. Huang, K. L. Li, T. T. Yu, Y. X. Zhang and D. Losic, *J. Mater. Chem. A*, 2015, **3**, 7855.

[16] H. Wang, Q. L. Zhao, X. Y. Wang, Y. W. Zhang, J. Gao, Y. Q. Fu, X. K. Yang and H. B. Shu, *RSC Adv.*, 2014, **4**, 42910.

[17] S. X. Sun, J. W. Lang, R. T. Wang, L. B. Kong and X. C. Li, *J. Mater. Chem. A*, 2014, **2**, 14550.

[18] Y. X. Zeng, Y. Han, Y. T. Zhao, Y. Zeng, M. H. Yu, Y. J. Liu, H. L. Tang, Y. X. Tong and X. H. Lu, *Adv. Energy. Mater.*, 2015, **5**, 1402176.

[19] J. X. Zhu, L. J. Cao, Y. S. Wu, Y. J. Gong, Z. Liu, H. E. Hoster, Y. H. Zhang, S. T. Zhang, S. B.

Yang, Q. Y. Yan, P. M. Ajayan and R. Vajtai, *Nano Lett.*, 2013, **13**, 5408.

[20] M. J. Zhi, C. C. Xiang, J. T. Li, M. Li and N. Q. Wu, *Nanoscale*, 2013, **5**, 72.

[21] N. N. Wang, Y. J. Zhai, X. J. Ma and Y. T. Qian, *RSC Adv.*, 2015, **5**, 611148.

[22] S. Y. Kim, H. M. Jeong, J. H. Kwon, I. W. Ock, W. H. Suh, G. D. Stucky and J. K. Kang, *Energy Environ. Sci.*, 2015, **8**, 188.

[23] Z. P. Li, J. Q. Wang, Z. F. Wang, Y. B. Tang, C.-S. Lee and S. R. Yang, *RSC Adv.*, 2014, **4**, 54416.

[24] C. Wei, P. S. Lee and Z. C. Xu, *RSC Adv.*, 2014, **4**, 31416.

[25] Z. Y. Zhang, F. Xiao, L. H. Qian, J. W. Xiao, S. Wang and Y. Q. Liu, *Adv. Energy Mater.*, 2014, **4**, 1400064.

[26] H. M. Zhang, D. Guo, J. Zhu, Q. H. Li, L. B. Chen and T. H. Wang, *Electrochim. Acta*, 2015, **152**, 378.

[27] Z. J. Su, C. Yang, B. H. Xie, Z. Y. Lin, Z. X. Zhang, J. P. Liu, B. H. Li, F. Y. Kang and C. P. Wong, *Energy Environ. Sci.*, 2014, **7**, 2652.

[28] X. H. Xia, J. P. Tu, Y. Q. Zhang, X. L. Wang, C. D. Gu, X.-B. Zhao and H. J. Fan, *ACS Nano*, 2012, **6**, 5531.

[29] D. Z. Kong, J. S. Luo, Y. L. Wang, W. N. Ren, T. Yu, Y. S. Luo, Y. P. Yang and C. W. Cheng, *Adv. Funct. Mater.*, 2014, **24**, 3815.

[30] D. D. Zhu, Y. D. Wang, G. L. Yuan and H. Xia, *Chem. Commun.*, 2014, **50**, 2876.

[31] K. B. Xu, W. Y. Li, Q. Liu, B. Li, X. J. Liu, L. An, Z. G. Chen, R. J. Zou and J. Q. Hu, *J. Mater. Chem. A*, 2014, **2**, 4795.

[32] K. Wang, Z. Q. Shi, Y. Y. Wang, Z. G. Ye, H. Y. Xia, G. W. Liu and G. J. Qiao, *J. Alloys*

Comp., 2015, **624**, 85.

[33] M. Huang, Y. X. Zhang, F. Li, L. L. Zhang, Z. Y. Wen and Q. Liu, *J. Power Sources*, 2014, **252**, 98.

[34] L. Yu, G. Q. Zhang, C. Z. Yuan and X. W. Lou, *Chem. Commun.*, 2013, **49**, 137.

[35] Y. Li, Z.-Y. Fu and B.-L. Su, *Adv. Funct. Mater.*, 2012, **22**, 4634.

[36] M. H. Yu, W. Wang, C. Li, T. Zhai, X. H. Lu and Y. X. Tong, *NPG Asia Mater.*, 2014, **6**, e129.

[37] M. H. Yu, Y. X. Zeng, C. Zhang, X. H. Lu, C. H. Zeng, C. Z. Yao, Y. Y. Yang and Y. X. Tong, *Nanoscale*, 2013, **5**, 10806.

[38] D. Q. Liu, Q. Wang, L. Qiao, F. Li, D. S. Wang, Z. B. Yang and D. Y. He, *J. Mater. Chem.*, 2012, **22**, 483.

Figure captions

Fig. 1 (a) XRD pattern of NiO and NiO@MnO_2. (b) EDS spectra of NiO@MnO_2.

Fig. 2 SEM images of (a) NiO and (b) NiO@MnO_2 with different magnifications. Inset is the locally enlarged image. (c) and (d) TEM images of a NiO@MnO_2 core-shell nanosheet scratched off the CFP with different magnifications. (e) HRTEM image and (f) the corresponding SAED pattern of NiO@MnO_2 nanosheet.

Fig. 3 (a) Nitrogen adsorption and desorption isotherms of NiO@MnO_2 nanosheet and (b) The corresponding Barrett-Joyner-Halenda (BJH) pore size distribution.

Fig. 4 (a) CV curves of NiO and NiO@MnO_2 nanosheet at the scan rate of 10 mV s^{-1}. (b) CV curves and (c) galvanostatic charge-discharge plots of NiO@MnO_2 core-shell nanosheet at different scan rates and current densities, respectively. (d) The corresponding specific and areal capacitance of NiO and NiO@MnO_2 nanosheet as a function of current density. (e) EIS Nyquist plots of NiO and NiO@MnO_2 nanosheet. The insets are the partial enlarged Nyquist plots. (f) Cycling performance of NiO@MnO_2 nanosheet electrode at current density of 20 mA cm^{-2}. The inset is the galvanostatic charge-discharge curves of last 17 cycles.

Fig. 5 (a) CV curves of the asymmetric supercapacitor at the scan rate of 50 mV s^{-1} in different applied potential windows. (b) CV curves and (c) galvanostatic discharge curves of the asymmetric supercapacitor at different scan rates and current densities, respectively. (d) The specific capacitance

of the asymmetric supercapacitor as a function of current density (e) Ragone plot of our supercapacitor device compared with other data. (f) Cycling performance and coulomb efficiency of the asymmetric supercapacitor at the current density of 4 A g^{-1}.

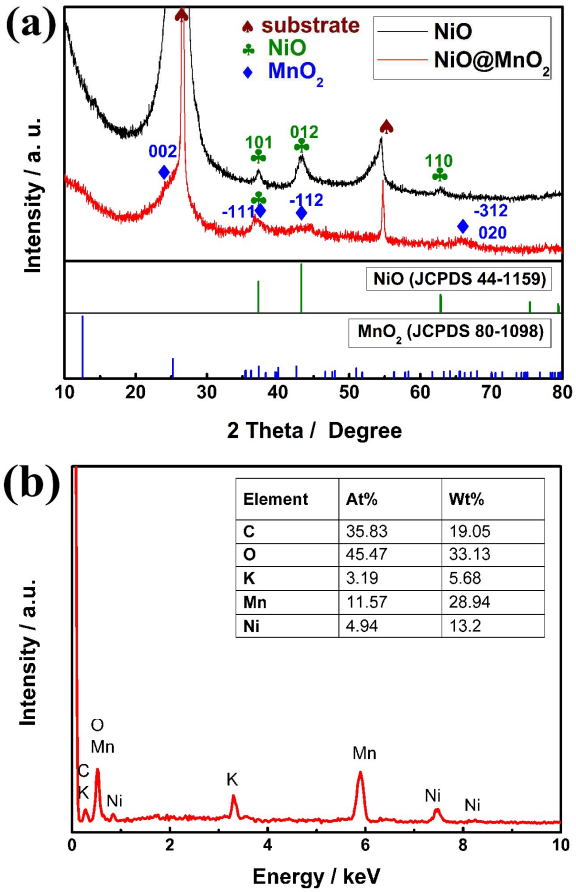

Fig. 1

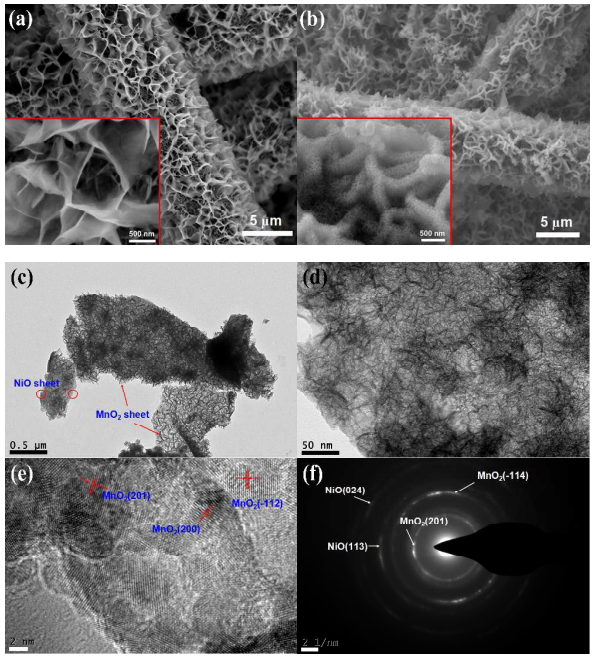

Fig. 2

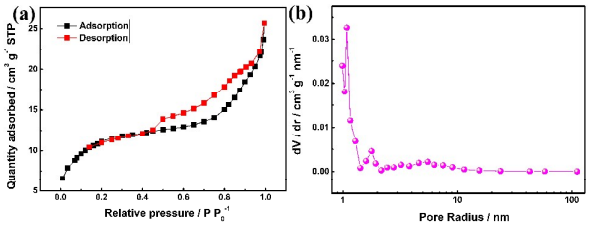

Fig. 3

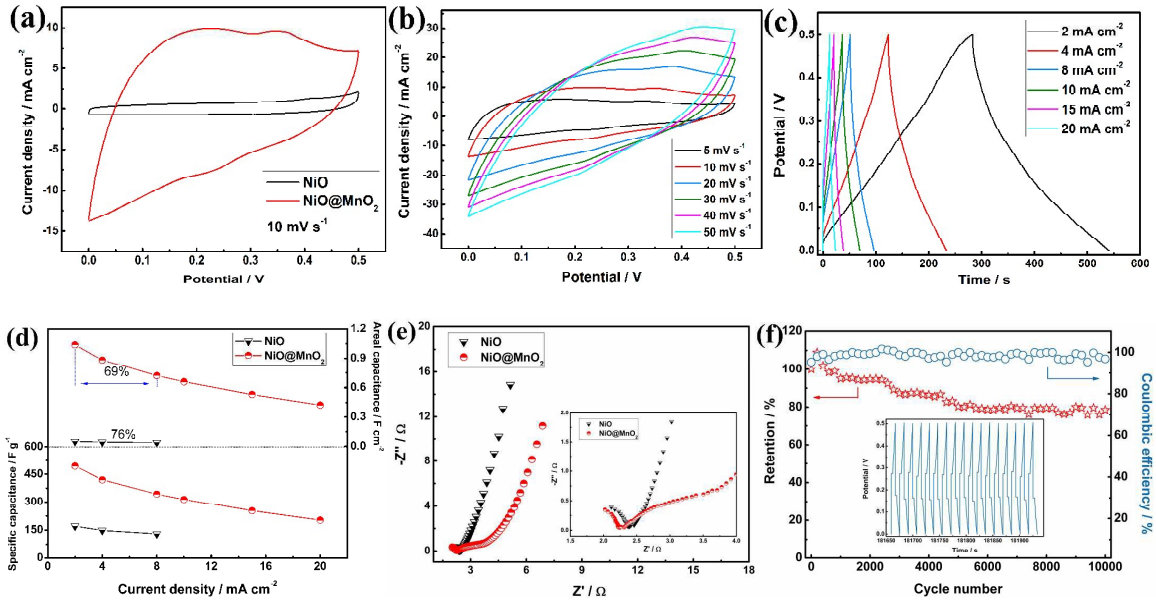

Fig. 4

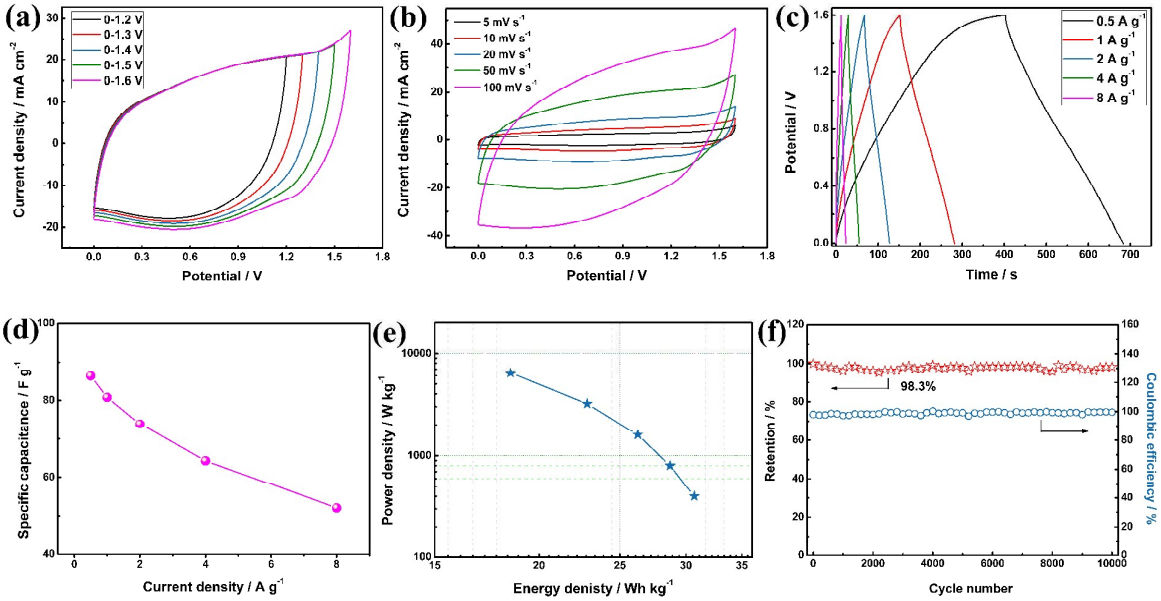

Fig. 5